ARTICLE OPEN

Check for updates

Suspension printing of liquid metal in yield-stress fluid for resilient 3D constructs with electromagnetic functions

Qian Wu[1,2], Fengbo Zhu[3], Ziliang Wu[4]✉, Yu Xie[5], Jin Qian[5]✉, Jun Yin[1,2]✉ and Huayong Yang[1]

Liquid metal is an ideal conductive material for soft electronics because of its high conductivity and fluidity at room temperature. However, the large surface tension and high mass density of liquid metal make forming three-dimensional (3D) dangling structures a challenging task. Reported here is a suspension printing strategy for direct deposition of galinstan-based liquid metal into 3D dangling structures with high shape fidelity and spatial resolution (~150 μm). Acrylamide/nanoclay suspension served as a yield-stress fluid support bath, with selected hydrogen peroxide to immediately oxidize the gallium skin and strengthen the extruded liquid metal, thus continuous liquid metal filaments were deposited successfully. The subsequent photo-curing of acrylamide/nanoclay works as a resilient outer packaging, giving rise to a ~500% tensile deformation for liquid metal-hydrogel composite. This suspension printing strategy should broaden the opportunity of using 3D and functional liquid metal constructs for soft yet resilient electromagnetic devices.

npj Flexible Electronics (2022)6:50 ; https://doi.org/10.1038/s41528-022-00184-6

INTRODUCTION

Soft and flexible electronics (e.g., smart sensors, actuators, and soft robotics), which can perform prescribed functions when subjected to large deformation, are increasingly valued compared to traditional rigid electronics. Among various materials to construct such functional devices, gallium (Ga)–based liquid metal alloys have drawn intensive attention, attributed to a combination of physical properties such as high electric conductivity, self-healing ability, fluidity, and low toxicity[1,2]. The central characteristic to make liquid metal alloys popular in flexible electronics is their ability to flow, leading to a continuous nature under a wide range of deformation[3]. To achieve the functionality of liquid metals in various applications, it is crucial to elaborately pattern liquid metals, typically in two-dimensional (2D) or three-dimensional (3D) configurations[4]. Although various patterning techniques have been developed in the past few years, including microfluidics[5,6], stencil lithography[7], transfer printing[8], and freeze-casting[9], these conventional manufacturing methods generally require additional pre- or post-treatments, such as preparation of masks, substrate surface modification, and post sintering. In contrast, additive manufacturing, as a speedily developing technology to produce complex internal structures and highly customized models[10,11], has been implemented to pattern liquid metals into both in-plane and out-of-plane architectures, including direct writing[12], droplet-by-droplet deposition[13], and roller-ball-pen printing[14]. However, current additive manufacturing strategies for liquid metals patterning are primarily confined to 2D planes, due to the intrinsic properties of liquid metals, such as high surface tension, high density, and low viscosity. The increasing demand of high-density integrated electronics capable of processing high-throughput information drives the need to fabricate arbitrary 3D interconnects, which is critical for further applications of liquid metals[15,16]. Compared to the 2D circuit, a 3D circuit with arbitrary configuration has obvious advantages in reducing device size and transmission loss, enhancing the mechanical stretchability and robustness of the device[6]. In addition, the ability to fabricate 3D structures of liquid metal is useful and necessary for many applications, such as complex microfluidics, electrical components, induction coils, antennas, electrodes, and flexible networks[9,17–19]. Therefore, how efficiently constructing deformable liquid metal interconnects in arbitrary 3D configurations becomes a demanding task of liquid metal fabrication[15].

Previous studies have shown that the high surface tension (~600 mN m^{-1})[20] and near-Newtonian behavior with low viscosity (2×10^{-3} Pa·s)[21,22] are the formidable obstacles for liquid metals to form continuous and uniform filaments by extrusion-based 3D printing methods[23], since Rayleigh–Taylor instability tends to take place[24], and leads to the break-up of cylindrical liquid metals into droplets. Although Ladd et al.[23] showed the feasibility of building free-standing 3D structures by stacking liquid metal droplets on top of each other, the coarse printing resolution and low printing reproducibility of droplet deposition are restricting liquid metals for highly integrated electronic devices. Recently, several studies made efforts to avoid droplet formation during liquid metal extrusion based on the property of liquid metals that rapidly reacts with oxygen to form a solid-like shell[25]. It has been observed that once exposed to the air, a solid-state surface of oxidized gallium, instantaneously forms on the outer surface of the liquid metal, creating a passivating oxide skin. The oxide skin is extremely thin (~1 nm)[26], and the rheological characteristics of the liquid metals, i.e., yield stress and elastic modulus, were found to be dominated by the interfacial mechanics of the skin rather than the bulk properties of the internal liquid metals[22]. During the printing, the oxide skin forms simultaneously as an elastic shell when the ink is extruded from the nozzle, which encapsulates the

[1]The State Key Laboratory of Fluid Power and Mechatronic Systems, School of Mechanical Engineering, Zhejiang University, Hangzhou 310028, China. [2]Key Laboratory of 3D Printing Process and Equipment of Zhejiang Province, School of Mechanical Engineering, Zhejiang University, Hangzhou 310028, China. [3]College of Materials Science & Engineering, Taiyuan University of Technology, Taiyuan 030024, China. [4]MOE Key Laboratory of Macromolecular Synthesis and Functionalization, Department of Polymer Science and Engineering, Zhejiang University, Hangzhou 310027, China. [5]Key Laboratory of Soft Machines and Smart Devices of Zhejiang Province, Department of Engineering Mechanics, Zhejiang University, Hangzhou 310027, China. ✉email: wuziliang@zju.edu.cn; jqian@zju.edu.cn; junyin@zju.edu.cn

liquid metal inside. Thus, the oxide skin can mechanically stabilize the extruded filament against capillary forces to maintain the printed 3D structures, which plays an integral role in the 3D printing of liquid metals[19]. Furthermore, Gannarapu et al.[3,27] presented a 3D-freeze printing to enable substantially higher structural stability than the oxide skin alone by dispensing liquid metals on a cooled substrate and frozen simultaneously to fabricate 3D structures without support materials. It should be noted that the electrical resistance of liquid metal remains largely unaffected because the oxide skin is much thinner than the surrounded liquid metal[23].

By taking advantage of the oxide skin, the patterning of liquid metals into 3D dangling structures was achieved by extrusion-based printing[28], mainly simple out-of-plane structures with vertical free-standing or horizontal bridge filaments[3,15,23], because the structural strength of the oxide skin is not sufficient to support 3D complex structures with high aspect ratios. The strategy of adding fillers to the liquid metal inks helps forming 3D structures at a height of millimeter-scale, but the printability and shape fidelity is limited by the gravity due to the lack of supporting materials[26]. To build more complex 3D structures with suspended, discrete or bent architectures, printing liquid metals with support materials is a more reliable approach. The technology of printing in a support bath has been utilized to print hydrogel[29–31], polydimethylsiloxane (PDMS)[32], and carbon conductive grease[33], affording high printing resolution and shape fidelity. Yu et al.[18] also reported a suspension 3D printing of liquid metal in self-healing carbopol hydrogel, but this method failed to print continuous liquid metal filaments in the support bath, only forming liquid metal droplets, since the oxide skin could not be formed due to the limited oxygen in the support bath, and the large interfacial tension between liquid metal and carbopol hydrogel drove liquid metal to form spherical shapes. Wang et al.[34] proposed an electrochemical method to create an oxide film on the surface of printed liquid metal and printed wire-like structures in the supporting hydrogel. However, their printed structures of liquid metal showed poor shape fidelity and low resolution (the minimum wire diameter is about 300 μm). Moreover, to work as flexible electronic devices, the printed liquid metal structures need to be separated from the support bath after printing and then encapsulated by elastomer, making the fabrication process more complicated.

In this work, galinstan was printed into selected acrylamide (AAm)/nanoclay suspension in the presence of hydrogen peroxide (H_2O_2), which worked as a support bath and enabled the extrusion of galinstan into continuous filaments with a diameter of 150 μm. The influences of hydrogen peroxide concentration, printing velocity, and extrusion flowrate on galinstan printability were systematically studied. For demonstration, circular helix, hourglass, and representative complex 3D dangling structures were manufactured by the freeform deposition of galinstan filaments in the suspension, which was subsequently cured to form a tough hydrogel serving as the envelope of the printed liquid metal structures. The electrical stability of printed circuits was characterized during the dynamic tensile testing, and the printed circuits remained intact for tensile strain up to 500%. The 3D helical structures of liquid metal embedded in the nanocomposite hydrogel were prototyped as a resonant sensor and an electromagnetic generator to produce induced voltage through magnet movement. The method demonstrated here should provide a promising strategy for manufacturing macroscopic 3D dangling structures of liquid metals, and promote the use of 3D liquid metal constructs in soft and flexible electronics.

Table 1. Herschel–Bulkley parameters of three AAm/nanoclay suspensions used in experiments.

H_2O_2 (%)	σ_y (Pa)	K (Pa·s^n)	n
0	115.92 ± 16.6	52.99 ± 10.7	0.390 ± 0.03
0.67	116.85 ± 20.3	40.79 ± 10.8	0.383 ± 0.05
1.33	112.61 ± 16.1	22.72 ± 6.0	0.462 ± 0.05

RESULTS

Rheological properties of the support bath

The rheological analysis of AAm/nanoclay suspensions with hydrogen peroxide concentrations of 0, 0.67 and 1.33% is shown in Supplementary Fig. 1. The trend of viscosity (η) decreasing with the shear rate ($\dot{\gamma}$) confirmed the shear-thinning character of the AAm/nanoclay suspensions. Notably, shear stress still existed as the shear rate approached zero, indicating that the AAm/nanoclay suspensions are yield-stress fluids. Also, the high similarity of three shear rate-shear stress ($\dot{\gamma} \sim \sigma$) curves indicated that H_2O_2 had no significant effect on the flow behavior of AAm/nanoclay suspensions. To quantitatively analyze the flow behavior of the suspensions, we fitted the measured $\dot{\gamma} \sim \sigma$ curves of three suspensions by Herschel–Bulkley model, i.e., $\sigma = \sigma_y + K\dot{\gamma}^n$, where σ_y is the yield stress, K is the consistency index, and n is the flow index, and the fitted parameters are summarized in Table 1. It is found that the fitting data are in good agreement with the measured data, and the yield stress of the three suspensions is low enough (~10^2 Pa), leading to a low mechanical resistance during the nozzle moving in the support bath. Thus, when $\sigma < \sigma_y$, the support bath behaves as a rigid body to support the printed structures in place. In contrast, when $\sigma \geq \sigma_y$, it behaves as a viscous fluid to allow the nozzle to move freely throughout the suspension and fill any crevice behind the nozzle. By comparing the yield stress of the support bath (σ_y) to the stress exerted on the support bath by the extruded ink, due to its gravity and buoyance, the scenario for extruded ink to be stable in the bath can be given by the threshold condition $\sigma_y A_n \geq Y_{crit}\Delta\rho V g$ (Fig. 1a), where A_n is the surface area of the ink, Y_{crit} is a dimensionless parameter associated with a yield stress, $\Delta\rho$ is the density difference between ink and support bath, V is the volume of extruded ink, and g is the acceleration due to gravity[35,36].

Furthermore, the material of the support bath should be fast-recovered, which is expected to rapidly recover its mechanical properties after a large-amplitude oscillatory breakdown. To quantify the recovery behavior of the AAm/nanoclay suspension, we performed three interval thixotropy tests (3ITT) with three consecutive intervals. Supplementary Fig. 1c shows the variation of storage modulus (G') and loss modulus (G'') during the test, and the curves of three AAm/nanoclay suspensions almost overlapped, suggesting that the recoverability of AAm/nanoclay suspensions was not affected by hydrogen peroxide. In the initial interval, the sample was subjected to a small amplitude of oscillatory shear (strain amplitude of 1% and frequency of 1 Hz) for 120 s to simulate behavior at rest; and the suspension exhibited a quasi-solid state ($\tan\delta = \frac{G''}{G'} \approx 0.03 - 0.05$). Subsequently, the sample was subjected to a strong shear (strain amplitude of 100% and frequency of 1 Hz) for 120 s to simulate the structural breakdown of the suspension during the printing process. The change of imposed strain caused the G' value to drop from 2 kPa to 30 Pa immediately and the G'' value to increase slightly from 100 to 175 Pa, making the suspension a quasi-liquid state ($\tan\delta \approx 4$–6). This result indicates that the suspension can change from a quasi-solid state to a quasi-liquid state as soon as the nozzle passes, which enables the nozzle to move freely in the suspension at any time. Finally, the same preset oscillatory shear of small amplitude

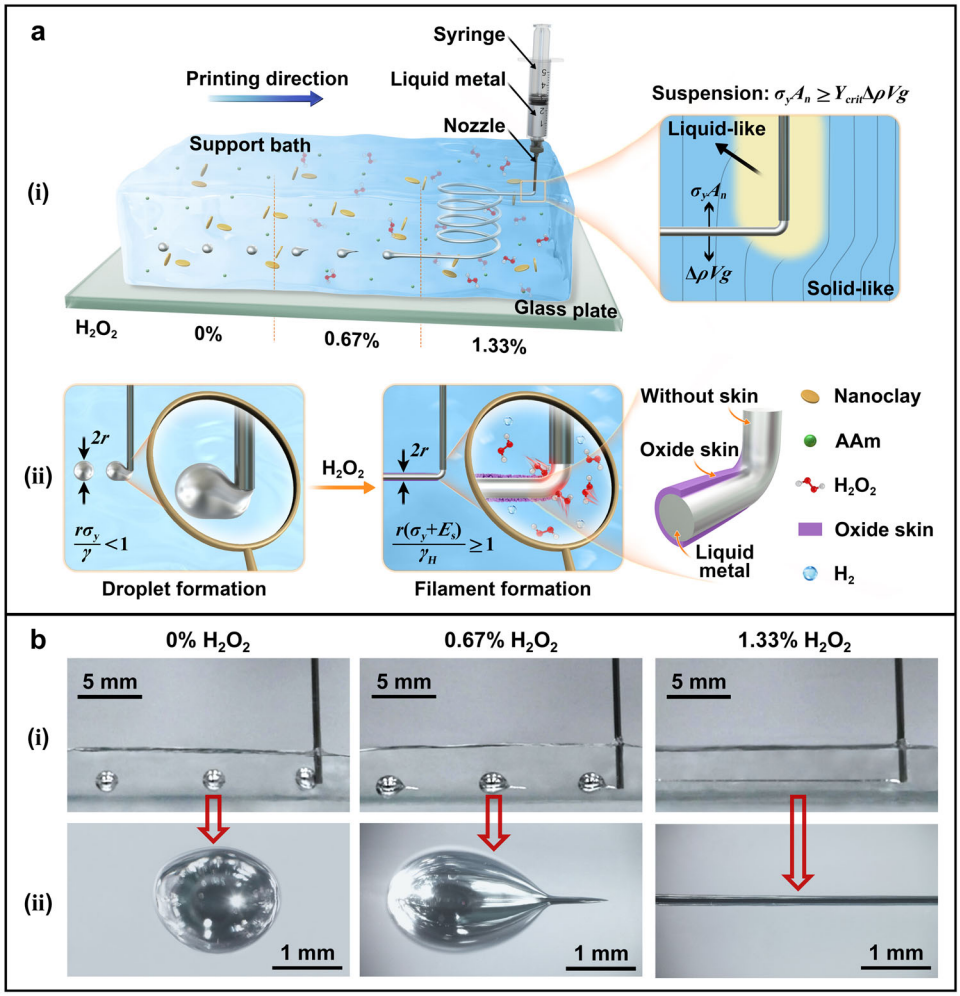

Fig. 1 The mechanism of printing liquid metal dangling structures in the AAm/nanoclay support bath. a Schematic of liquid metal suspension printing in AAm/nanoclay support bath with hydrogen peroxide. **b** Influence of hydrogen peroxide concentration on the printed filaments. (i) and (ii) show photographs and optical microscope images of a linear configuration of liquid metal printed in the support bath with different hydrogen peroxide concentrations, respectively.

as in the first interval was used to simulate structural regeneration at rest after printing. G' and G'' quickly recovered to their initial values and kept this quasi-solid state ($\tan\delta \approx 0.03$–0.05) for a long time. This fast-recovery capability is significant for suspension 3D printing, indicating that the support bath can support the deposited filaments in place after the nozzle is moved away, which was the case in our experiments.

Effect of H_2O_2 concentration on liquid metal printability

During the extrusion printing in the support bath, the interfacial tension between the ink and the support bath caused an internal and external pressure difference, which tended to destabilize the deposited filaments through the mechanism of Rayleigh–Plateau instability[37,38]. According to the Young–Laplace equation, a cylindrical liquid metal filament with the radius of r (~100 μm) breaks into discrete droplets in the support bath when $\frac{r\sigma_y}{\gamma}<1$, where γ is the interfacial tension between the liquid metal and the support bath (Fig. 1a). In the pure AAm/nanoclay suspension (support bath without H_2O_2), the large interfacial tension between the liquid metal and the pure AAm/nanoclay suspension (γ ~500 mN m^{-1}, Supplementary Fig. 2c) and low yield stress (σ_y ~10^2 Pa) result in $\frac{r\sigma_y}{\gamma}\sim 10^{-2}<1$, so only discrete droplets can be deposited in the support bath without hydrogen peroxide. For our experiments, when the hydrogen peroxide was added to AAm/nanoclay suspensions, the elastic oxide skin formed on the surface of deposited liquid metal made it difficult to be broken. The oxide skin increased the force required to break the liquid metal filament because of the stiffness of the oxide skin (E_s ~10^5 Pa)[16] and reduced the interfacial tension between the liquid metal and the AAm/nanoclay suspension (γ_H ~250 mN m^{-1}, Supplementary Fig. 2c), corresponding to $\frac{r(\sigma_y+E_s)}{\gamma_H}\sim 10>1$, thus it enabled the formation of continuous liquid metal filaments in our experiments (Fig. 1).

Supplementary Fig. 2 shows the representative advancing contact angles (Supplementary Fig. 2a, b) and the interfacial tension (Supplementary Fig. 2c) between liquid metal droplets and the AAm/nanoclay suspensions with hydrogen peroxide concentrations of 0, 0.67, and 1.33%. It was found that the advancing contact angle of the liquid metal on the AAm/nanoclay suspension surface decreased from 154.374° ± 2.100° to 123.848° ± 4.076° as the hydrogen peroxide concentration of the suspension increased from 0 to 1.33%. The interfacial tension between the liquid metal droplet and the AAm/nanoclay suspension decreased with the increasing hydrogen peroxide concentration as well, from 500 mN m^{-1} to 250 mN m^{-1}. Therefore, liquid metal

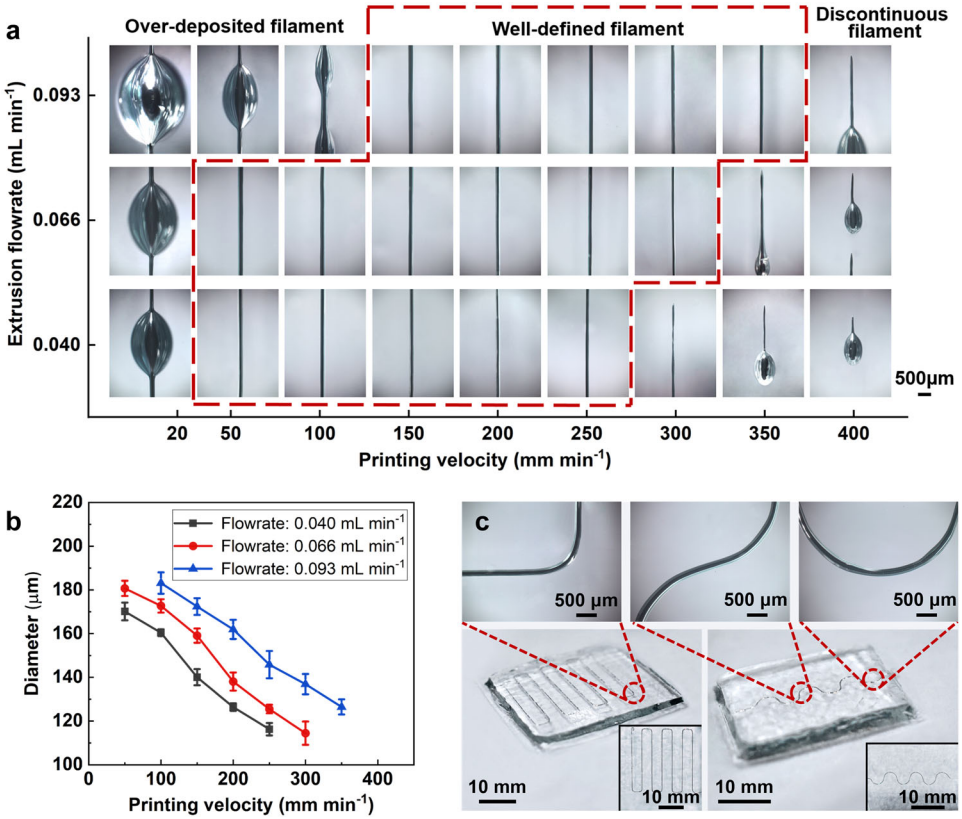

Fig. 2 The influence of printing conditions on filament formation. a Optical microscope images of liquid metal filaments resulted from different combinations of printing conditions. **b** Effects of printing velocity and extrusion flowrate on the resultant filament diameter. The error bars represent the standard deviation (s.d.). **c** Photographs and optical microscope images of representative printed patterns of liquid metal in the support bath. Inset: top-view photographs.

reacted rapidly with hydrogen peroxide in our printing to form an oxide skin, resulting in a decrease in the advancing contact angle and the interfacial tension between liquid metal and the AAm/nanoclay suspension effectively, which were beneficial factors to the formation of liquid metal filaments.

To further demonstrate the role of hydrogen peroxide in the suspension printing, liquid metal was printed in the AAm/nanoclay suspension with different hydrogen peroxide concentrations (0, 0.67, and 1.33%) under the same experimental condition (printing velocity of 100 mm min^{-1}, extrusion flowrate of 0.040 mL min^{-1}). As shown in Fig. 1b, in the suspension without (0%) hydrogen peroxide or with 0.67% hydrogen peroxide concentration, the liquid metal was deposited discontinuously as droplets along the printing path. The shape of liquid metal droplets varied from spheroidal (0% H_2O_2) to tadpole-like (0.67% H_2O_2). After further increasing the hydrogen peroxide concentration to 1.33%, continuous liquid metal filaments were extruded in the support bath. After being deposited in the support bath, a larger interfacial tension between the liquid metal and the support bath and small yield stress ($\frac{r\sigma_y}{\gamma} < 1$) forced liquid metal without oxide skin to form droplets in the support bath, while sufficient hydrogen peroxide in the support bath reacted rapidly with liquid metal at the tip of the nozzle, and an oxide skin formed instantaneously at the interface successfully resisted the interfacial tension between the liquid metal and the support bath. Further increasing the hydrogen peroxide concentration in the support bath to 2.00% had no greater effect on liquid metal printing (Supplementary Fig. 3). Therefore, AAm/nanoclay suspension with 1.33% hydrogen peroxide was utilized as an oxidated support bath to form stable and uniform liquid metal filaments along the printing path.

Effect of printing conditions on liquid metal printability

Printing conditions, including printing velocity, extrusion flowrate, and nozzle inner diameter, significantly affect the printing resolution and shape fidelity of liquid metal filaments. As shown in Fig. 2a, three representative filaments (over-deposited filament, well-defined filament, and discontinuous filament) were observed when the liquid metal was printed with a 24-gauge nozzle in the support bath with 1.33% H_2O_2 by varying extrusion flowrate and printing velocity. The over-deposited filaments were continuous yet highly heterogeneous with one or more spindle-shaped liquid metals, which were observed when the printing velocity was below 20 mm min^{-1}, or the extrusion flowrate was above 0.093 mL min^{-1}. On the contrary, discontinuous or multi-segmented filaments with irregular shapes were observed when the printing velocity was above 400 mm min^{-1} or the extrusion flowrate was below 0.040 mL min^{-1}. Each segment started with the accumulated liquid metal, and the diameter of the filament decreased with the printing path until it broke. The well-defined filaments were continuous and uniform, which can only be obtained at a moderate printing velocity and extrusion flowrate. In the operating region where well-defined filaments can be printed, the average diameter of printed liquid metal filaments increased with the extrusion flowrate and decreased with the printing velocity, while the average diameter of printed filaments was 120–190 μm under different printing conditions (Fig. 2b). As shown in Fig. 2c, the present method can print continuous,

uniform, and polyline/wavy profiles of liquid metal filaments with high shape fidelity in the support bath within the operating space (printing velocity of 100 mm min^{-1}, extrusion flowrate of 0.040 mL min^{-1}).

Validation of 3D printing of liquid metal constructs

The capability of printing liquid metals into complex 3D structures with continuous filaments is the key to further application of liquid metals in flexible electronic devices, and the demonstrations of 3D printed structures in the support bath were obtained under a printing velocity of 100 mm min^{-1} and extrusion flowrate of 0.040 mL min^{-1}. It should be noticed that previous studies[15,23] can only 3D print liquid metal into structures with a whole scale in micron, but this work presents the printing of 3D dangling structures of liquid metal with a high aspect ratio. Moreover, the polyacrylamide (PAAm)/nanoclay network formed by UV polymerization and photo-crosslinking of AAm contained in the support bath becomes a flexible sealing of printed liquid metal (Fig. 3a), making the printed liquid metal structures become deformable interconnects. Figure 3b, c show a circular helix structure with a pitch of 2 mm (see Supplementary Movie 1 for printing process), and Fig. 3d, e present a continuous double-layered structure with a vertical distance of 2.5 mm between two layers. Moreover, an hourglass structure (Fig. 3f–i) and complex 3D structures consisting of one (Fig. 3j–m) or two (Fig. 3n–q) irregular trajectories were printed in the support bath. The printed liquid metal was deposited stably along the defined paths, and all structures were stable during the printing process without collapsing, which exemplifies the reliability of this method in printing 3D dangling structures. After the polymerization of AAm/nanoclay suspension, the printed structures were connected to circuits with light-emitting diodes (LEDs) to verify their electrical conductivity, and all the light of LEDs successfully showed the high conductivity of printed liquid metal in the support bath. Thus, these examples confirmed the feasibility and flexibility of the suspension 3D printing method in fabricating macroscopic 3D suspended circuits using liquid metal.

Liquid metal-hydrogel electronics as a strain sensor

For the applications as soft and flexible electronic devices, the printed geometrically continuous liquid metal filaments embedded in the nanocomposite hydrogel should also be evaluated by their deformability and conductivity. Therefore, the resistance of liquid metal filaments with three configurations (line, sin wave, and polyline) encapsulated in PAAm/nanoclay hydrogel (Fig. 4a) was measured during stretching by dynamic tensile tests. It was noticed that the AAm contained in the support bath was polymerized and photo-crosslinked into the PAAm network by UV light, leading to a highly stretchable hydrogel with 1400% strain (Fig. 4b). As a demonstration, a PAAm/nanoclay hydrogel embedded with a sin-wave configuration liquid metal filament was connected to a yellow LED circuit to test the conductivity of printed liquid metal under tension. The result in Fig. 4a indicated that the LED worked well under the stretch strain of 500%, confirming that the printed filaments were continuous and conductive throughout the tensile process. Three printed configurations with an undeformed resistance around 1 Ω, and maintained an overall low resistance (<10 Ω) while being stretched up to 500% strain. Figure 4c illustrates the quantitative relationship between relative resistance change ($\Delta R/R_0$) and applied strain (ε). The slope of the $\Delta R/R_0$–ε curves reflects the gauge factor ($\mathrm{GF} = \frac{d(\Delta R/R_0)}{d\varepsilon}$) of the liquid metal-hydrogel electronics as a strain gauge, which is a key indicator for evaluating the performance of strain sensing. The relative resistance change increased linearly with the strain up to 200%, and approximate GF values of 1.20, 0.36, and 0.28 were extracted for the line, sin wave, and polyline configurations, respectively. When the hydrogel matrix was at the same uniaxial strain level, the gauge factor was more pronounced for the line configuration due to the lower mechanical stretchability, since the effective deformation of the embedded line configuration was remarkably higher compared to that of the sin wave and polyline configurations. Thus, the line configuration is more suitable for sensing due to its higher *GF* value, while the polyline configuration is more suitable as resilient interconnects. Moreover, a cyclic tensile test of 250 cycles (0 to 100% tensile strain) was performed to investigate the electrical stability and mechanical durability of the liquid metal-hydrogel electronics during extended stretching. The results show that the change in resistance of the liquid metal-hydrogel electronics remained stable (only a 6.5% change) during the first 80 stretching cycles of 5 h (Fig. 4d), but the resistance gradually increased until it failed (250 cycles, Supplementary Fig. 4). The dehydration and irregular shrinkage of the hydrogel during the test resulted in the squeezing of the sealed liquid metal circuit, which led to the increase in device resistance (Supplementary Fig. 5b). Therefore, how to maintain the humidity of the hydrogel to ensure the electrical stability of the liquid metal-hydrogel electronics is of great importance.

Liquid metal-hydrogel electronics for electromagnetic function

Resonant sensors have extensive applications in soft robots, wearable devices, and implantable sensors because of their passive and wireless advantages[39–41]. A passive resonant sensor with kirigami patterning designed by ref. [42] can detect deformation of materials in closed systems, promising for wearable biomonitoring and untethered robotics. However, the initial pattern of the resonant sensor in their study is 2D, which can only monitor the tensile deformation in the system but not the compressive deformation, thus limiting its application to a certain extent. Moreover, the conductive traces of the resonant sensor were made of copper, which limited the deformability and repeatability of the sensor due to its limited ductility and fatigue. Here, we fabricated a wireless resonant sensor based on a 3D liquid metal structure, which can monitor both tensile and compressive deformations.

To evaluate the performance of a liquid metal-hydrogel-based-resonant sensor, we measured the reflection (S11) of the electronics at rest, compression, and tension states by a vector network analyzer (miniVNA Tiny Plus2). Figure 5a presents the specimen and device used for the resonant sensor test. A circular Archimedean helix structure was printed using liquid metal in the support bath (printing velocity of 100 mm min^{-1}, extrusion flowrate of 0.066 mL min^{-1}) with a fixed inner diameter of 4 mm, an outer diameter of 20 mm, and height of 8 mm. The horizontal (P) and vertical (H) distances of adjacent spirals in the Archimedean helix were varied to investigate the response of different structures to compression and tensile strains. To test the resonance frequency variation (Δf) of the resonant sensor, we placed the printed liquid metal-hydrogel resonant sensor between two glass plates, which was subjected to an axial compression load or an axial tension load. Figure 5b–d show the reflections (S11) of three different sensors ($P = H = 0.8$ mm, $P = H = 1.6$ mm and $P = H = 2.4$ mm) in the frequency range from 1 MHz to 3 GHz under the strain ranging from −50% (compression) to 50% (tensile). It was found that the resonance frequency (i.e., the frequency at the maximum of reflection) of the sensors at rest increased with P and H. For the same configuration, when subjected to a compressive or tensile strain, the geometric variation of the spiral distribution led to the change of inductance (L) and capacitance (C), which resulted in a resonance frequency shift of the sensor. Therefore, the resonant frequency of the present 3D Archimedean spiral resonant sensor decreased with

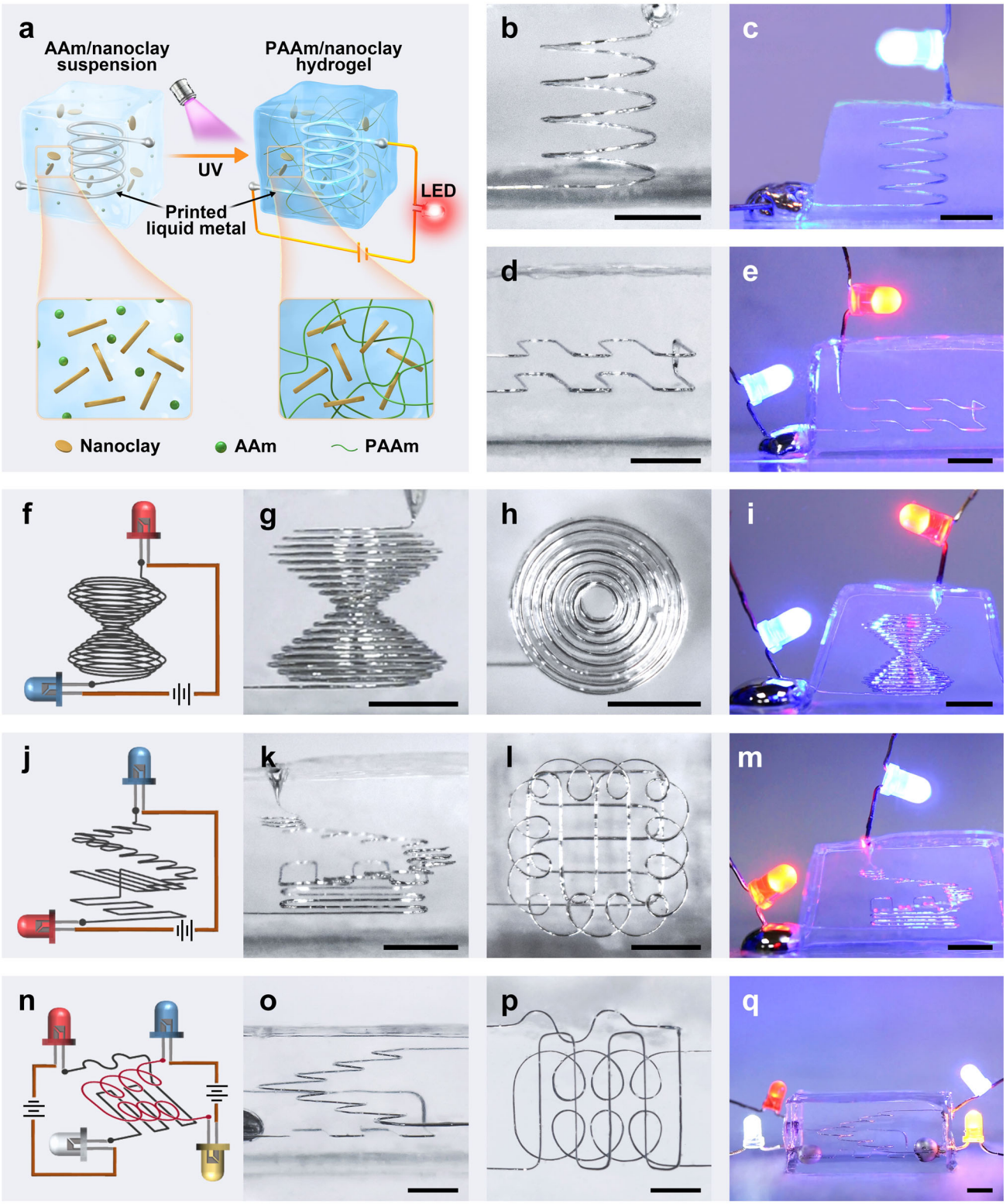

Fig. 3 Liquid metal-hydrogel electronics with printed dangling structures of liquid metal. a Schematic of AAm/nanoclay suspension polymerized into PAAm/nanoclay hydrogel under ultraviolet light after printing. **b**–**q** Printed 3D structures of liquid metal after printing and at work: **b**, **c** Circular helix structure. **d**, **e** Double-layered structure. **f**–**i** Hourglass structure. **j**–**q** Designed structures with one (**j**–**m**) or two (**n**–**q**) interlacing circuits. Scale bars: 5 mm.

compression strain or increased with tensile strain. Figure 5e illustrates the change of the resonant frequency of resonant sensors under different values of strain. The response of the resonant sensor to the same strain was more significant with a larger 3D feature (greater P and H values), which demonstrated the efficiency of a 3D resonant sensor for tensile and compression detection. For instance, at −50% strain, the resonant frequency of the resonant sensor with $P = H = 2.4$ mm decreased about 0.4 GHz

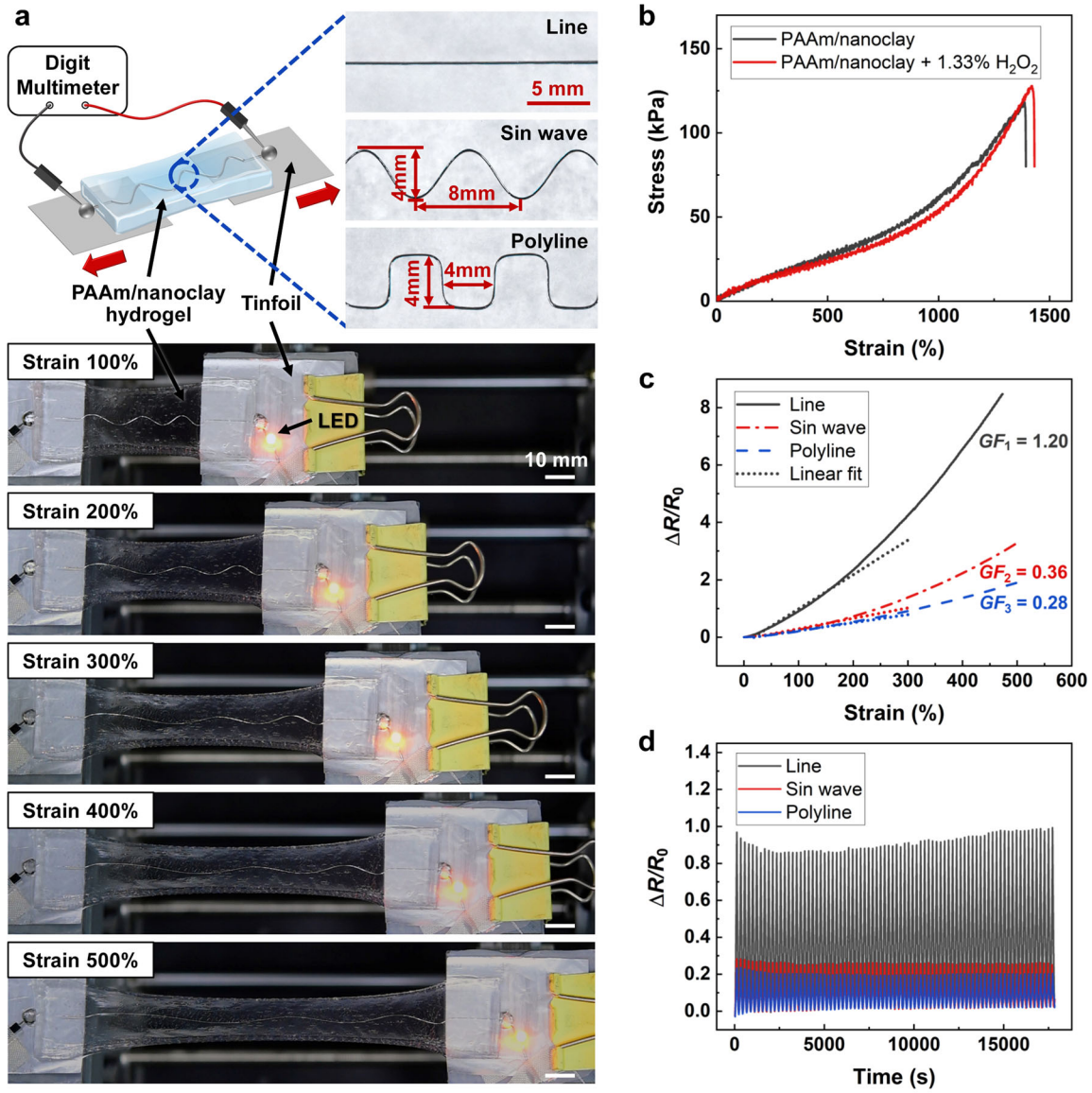

Fig. 4 Characterization of tensile electrical properties of liquid metal-hydrogel electronics. a Schematic of tensile test and photos of three configurations of liquid metal circuits in the PAAm/nanoclay hydrogel, and snapshots of the hybrid hydrogel with printed sin-wave liquid metal at different tensile strains. The liquid metal-hydrogel electronics was connected to a yellow LED to show the working state. **b** Tensile stress-strain curves of PAAm/nanoclay hydrogel, without and with 1.33% H_2O_2. **c** Relative resistance change as a function of tensile strain for liquid metal-hydrogel electronic devices with three configurations. **d** The relationship between relative resistance change and time for liquid metal-hydrogel electronic devices with three configurations during the first 80 cycles of stretching.

from the initial frequency, but the resonant frequency of the sensor with $P = H = 0.8$ mm only decreased about 0.2 GHz. The linear response to compression strain of the resonant sensor with a printed 3D helix reflects showed its potential for wireless pressure monitoring.

The electromagnetic generator is another application of the present liquid metal-hydrogel electronics with a 3D structure. Here, the device in Fig. 5f was used to detect the induced electromotive force (EMF) generated by a moving magnet inside a printed liquid metal coil and a copper coil, respectively. The liquid metal spiral coil with a diameter of 18 mm and a pitch of 0.8 mm was printed in a hollow square support bath and connected to a digital multimeter, and a cylindrical neodymium-iron-boron (NdFeB) magnet (N35) with a diameter of 8 mm and a height of 20 mm was vertically moved inside the coil at constant speeds of 150, 300, and 380 mm s^{-1}, respectively. As shown in Fig. 5g, the induced EMF with stable values was generated in the printed liquid metal coil due to the electromagnetic induction of the moving magnet. More importantly, the value of EMF effectively increased with the speed of the moving magnet due to the increased variation rate of the magnetic flux around the coil. Also, the same induced EMF was generated in the copper coil with similar geometry (Fig. 5h). It was found that a maximum voltage of 10 mV was produced by the liquid metal coil at a magnet moving speed of 380 mm s^{-1}, which was comparable to the results of the copper coil group. In addition, the power delivered by the electromagnetic generator to a resistive load of 5 Ω was tested (Supplementary Fig. 6), which is an important indicator of the electromagnetic generator. As shown in Fig. 5i, j, the maximum power delivered by the liquid metal coil electromagnetic

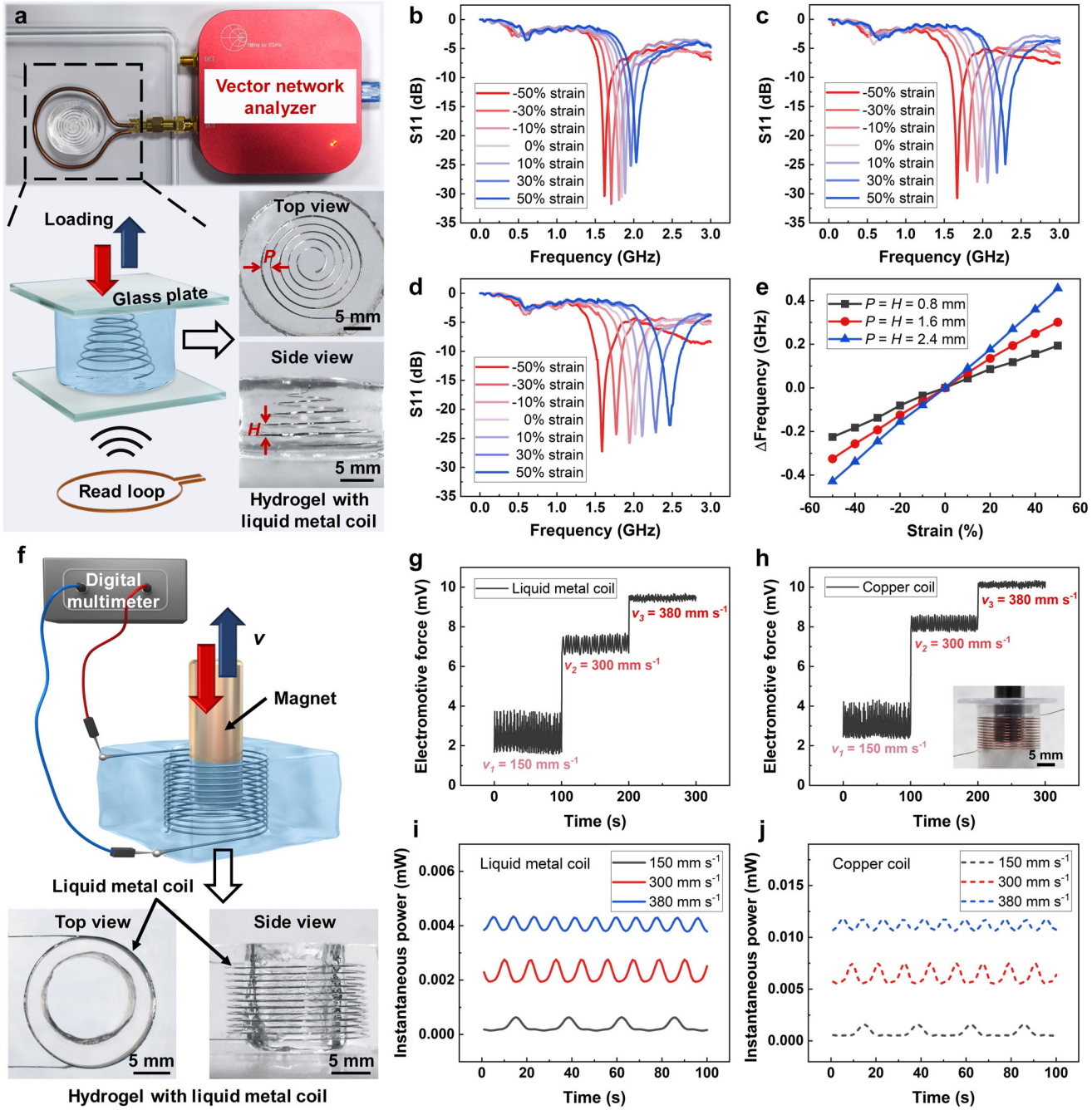

Fig. 5 Liquid metal-hydrogel electronics for electromagnetic functions. a Liquid metal-hydrogel specimens and device used for the resonant sensor test. **b**–**d** The reflection (S11)-strain relationship of three sensors. **b**–**d** show S11 of the sensors with $P = H = 0.8$ mm, $P = H = 1.6$ mm, and $P = H = 2.4$ mm, respectively. **e** The variation of resonant frequencies of the hydrogel embedded with a liquid metal of three configurations under different levels of compressive and tensile strain. **f** Liquid metal-hydrogel specimens and device used for the electromagnetic induction test. **g**, **h** Induced EMF generated by a liquid metal coil (**g**) and a copper coil (**h**, for comparison) at different moving speeds of the permanent magnet. **i**, **j** The power is delivered to a resistive load (5 Ω) of the electromagnetic generators with a liquid metal coil (**i**) and a copper coil (**j**) at different frequencies.

generator to the resistive load is about 0.004 mW, while that of the copper coil is about 0.012 mW. The difference in delivered power is due to the difference in resistance between the copper coil and the liquid metal coil. The resistance of the printed liquid metal coil is 4.13 Ω, which is about 11 times of the fabricated copper coil (0.38 Ω), despite their similar geometry. Therefore, the lower power delivered from the liquid metal coil electromagnetic generator than the copper coil electromagnetic generator to a resistive load of 5 Ω is reasonable. The successful response of the printed liquid metal coil to varying magnetic fields demonstrated the ability of liquid metal-hydrogel electronics to produce induced EMF, which is promising for the fabrication of electromagnetic generators or other devices with complex 3D conductor structures.

DISCUSSION

This work reported the macroscopic 3D dangling structures of galinstan-based liquid metal, manufactured with high shape fidelity by extrusion printing in a customized support bath. The addition of 1.33% H_2O_2 in the AAm/nanoclay suspension significantly changed the rheological properties and interfacial tension between liquid metal and the AAm/nanoclay suspension, leading to the instantaneous formation of a viscoelastic oxide skin on the extruded liquid metal surface. Consequently, continuous filaments (~150 μm in diameter) of liquid metal can be successfully deposited into 3D constructs with the selection and control of printing velocity and extrusion flowrate. The shape fidelity of liquid metal in AAm/nanoclay suspension with 1.33% H_2O_2 was demonstrated by printing complicated 3D dangling structures, including circular helix and hourglass structures against gravity due to the supporting role of the suspension. The superior deformability of PAAm/nanoclay hydrogel (tensile strain up to 1400%) and electrical properties of liquid metal endow the liquid metal-hydrogel hybrid with the ability of sensing large and repeated deformation. Moreover, the liquid metal-hydrogel electronics with a helical structure was used as a flexible resonant sensor, which can precisely monitor deformation in the range of −50% compressive strain to 50% tensile strain. A liquid metal coil printed in PAAm/nanoclay hydrogel generated a voltage of 10 mV, induced by electromagnetic coupling through a moving magnet, which is promising as an electromagnetic generator. This study provides an effective method for 3D printing of liquid metal structures with a high aspect ratio and facile fabrication of liquid metal-hydrogel flexible electronics, which may promote the application of liquid metals in soft and flexible electronics.

METHODS

Preparation of AAm/nanoclay support bath

Acrylamide (AAm) was obtained from Aladdin Industrial Corporation, Laponite nanoclay (Laponite XLG) was obtained from BF (Guangzhou, China), hydrogen peroxide (H_2O_2; 30 wt.% aqueous solution) was obtained from Sinopharm Chemical Reagent Co., Ltd (Shanghai, China), and polyethylene (glycol) diacrylate (PEGDA, MW ~700) was obtained from Sigma-Aldrich. Lithium phenyl-2,4,6-trimethylbenzoylphosphinat (LAP) was synthesized as described before[43,44] and used as the ultraviolet (UV) photoinitiator. The support bath was prepared by dissolving the prescribed amount of AAm (40%, w v^{-1}), LAP (1.0 wt%, relative to AAm), and PEGDA (0.28%, v v^{-1}) in water to form an aqueous solution in the dark at room temperature. Then, Laponite nanoclay powder (9.0%, w v^{-1}) was added into the AAm solution, which was kept stirring for more than 60 min to ensure thorough hydration of the nanoclay powder to generate homogeneous AAm/nanoclay precursor suspension. The suspension was stored in the dark in sealed containers at 4 °C to prevent polymerization and evaporation, and aged for one day before use. Prior to printing, 6 wt% H_2O_2 solution was added into the AAm/nanoclay precursor suspension in a volume ratio of 1:3.5 and mixed for 30 min to obtain the AAm/nanoclay support bath containing 1.33 wt% H_2O_2. Subsequently, the mixed solution was centrifuged (Sorvall ST8 Centrifuge) for 2 min at room temperature, at 4000 rpm, to remove the bubbles inside. Finally, the solution was carefully transferred to a glass plate as a support bath for further printing.

Rheological characterization of support bath

The rheological properties of AAm/nanoclay suspensions with different concentrations of hydrogen peroxide (0, 0.67%, and 1.33%) were characterized at 20 °C using a rheometer (MCR302, Anton Parr, Austria). A 25-mm-diameter parallel plate was used in all measurements. Prior to rheological characterization, the samples were placed between the parallel plate and the platform with a gap distance of 1 mm with special care to avoid bubbles. To quantitatively acquire the flow curves and determine the yield stress of the AAm/nanoclay suspensions, we performed steady rate sweeps over shear rates from 0.001 to 1000 s^{-1}. To investigate the recovery property of the AAm/nanoclay suspensions, three interval thixotropy tests (3ITT) were performed at a frequency of 1 Hz, and the oscillatory shear mode was used under a small strain of 1% for 120 s, then by a large strain of 100% for 120 s, and finally by a small strain of 1% for 300 s.

Table 2. Printing parameters used for direct writing of liquid metal.

Parameter	Values
Printing velocity (mm min^{-1})	20, 50, 100, 150, 200, 250, 300, 350, 400
Extrusion flowrate (mL min^{-1})	0.040, 0.066, 0.093
Nozzle inner dimeter (mm)	0.26
Syringe inner diameter (mm)	13
Nanoclay concentration (% (w v^{-1}))	9.0
Hydrogen peroxide concentration (% (w v^{-1}))	0, 0.67, 1.33
AAm concentration (% (w v^{-1}))	40.0
Room temperature (°C)	20–25

Mechanical characterization of PAAm/nanoclay hydrogels

The PAAm/nanoclay hydrogel was obtained by the photo-crosslink of the AAm/nanoclay suspension under ultraviolet (UV) light irradiation. Tensile tests were performed by a commercial tensile tester (Instron 3343 Tester) with a stretch velocity of 100 mm min^{-1} at room temperature. The samples for testing were prepared in dumbbell shape with an initial gauge length of 12 mm, a width of 4 mm, and a thickness of 2 mm.

Preparation and characterization of liquid metal ink

The eutectic alloy of gallium (59.9%), indium (23.2%), and tin (16.9%) (Galinstan, Yantai Aibang Electronic Materials Co., Ltd. China) was used as the liquid metal ink. The melting point and density of liquid metal ink were measured to be 11 °C and 6.5 g cm^{-3}, respectively.

Extrusion-based printing of liquid metal in support bath

The setup of the printing system was shown in Fig. 1a, which consists of a material extrusion system with a syringe pump for extruding liquid metal ink through the nozzle at a constant flowrate Q and a three-axis positioning stage with automatic movements in the x, y, or z axis for controlling the motion of nozzle and support bath. The liquid metal ink was continuously extruded in the support bath at room temperature, and filaments were deposited along the printing path to form 2D patterns or 3D structures. During the extrusion printing, a 24-gauge (0.26 mm inner diameter) nozzle and a plastic syringe with 5 mL capacity (~13 mm inner diameter) were used, and the influence of printing velocity and extrusion flowrate were investigated. Here, the printing velocity varied from 20 to 400 mm min^{-1}, and the extrusion flowrate varied from 0.040 to 0.093 mL min^{-1}. Then, the support bath with printed liquid metal ink was polymerized under UV light (365 nm, 17 mW cm^{-2}) for 20 s. All the printing parameters are listed in Table 2.

Characterization of printed liquid metal-hydrogel samples

For the tensile test, galinstan was printed as line, sin wave, or polyline configurations within a rectangular support bath (45 mm × 20 mm × 4 mm). A speed-controlled motion stage consisting of a motor and a guide rail was used to continuously stretch the sample at a constant stretching rate of 0.18 mm s^{-1}, and a two-probe digital multimeter (34465 A, Keysight Co., Ltd) was used to measure and record resistance variations of the samples with imposed strain (Fig. 4a). The initial resistance (R_0) and the resistance change under applied tensile strain ($\Delta R = R - R_0$) were measured, and relative resistance variation was calculated as $\Delta R/R_0$. In order to evaluate the mechanical durability of liquid metal-hydrogel electronics, the specimens were subjected to 250 times cycling tensile test under a strain amplitude up to 100%.

Images of printed samples were taken using a digital camera (Nikon) under bright-filed. The diameters of filaments were measured in inverted optical microscope images.

Statistical analyses

All quantitative values of measurement and fitting in the figures and tables were reported as means ± standard deviation (SD), unless stated otherwise. The diameter of the filament represents the average of six filaments and five regions per filament (in total, 30 regions), and the values of other experiments represent the average of three samples in each group. Statistical analysis was performed using analysis of variance (ANOVA) and p-values of less than 0.05 were considered statistically significant.

DATA AVAILABILITY

All data generated or analyzed during this study are included in this published article (and its supplementary information files).

Received: 6 January 2022; Accepted: 2 June 2022;
Published online: 21 June 2022

REFERENCES

1. Dickey, M. D. Stretchable and soft electronics using liquid metals. *Adv. Mater.* **29**, 1606425 (2017).
2. Saborio, M. G. et al. Liquid metal droplet and graphene co-fillers for electrically conductive flexible composites. *Small* **16**, 1903753 (2019).
3. Gannarapu, A. & Gozen, B. A. Freeze-printing of liquid metal alloys for manufacturing of 3D, conductive, and flexible networks. *Adv. Mater. Technol.* **1**, 1600047 (2016).
4. Ma, B. et al. A versatile approach for direct patterning of liquid metal using magnetic field. *Adv. Funct. Mater.* **29**, 1901370 (2019).
5. Liu, S. et al. Can liquid metal flow in microchannels made of its own oxide skin? *Microfluid. Nanofluid.* **20**, 3 (2016).
6. Liu, H. et al. Biofriendly, stretchable, and reusable hydrogel electronics as wearable force sensors. *Small* **14**, 1801711 (2018).
7. Lazarus, N., Bedair, S. S. & Kierzewski, I. M. Ultrafine pitch stencil printing of liquid metal alloys. *ACS Appl. Mater. Interfaces* **9**, 1178–1182 (2017).
8. Guo, R. et al. One-step liquid metal transfer printing: toward fabrication of flexible electronics on wide range of substrates. *Adv. Mater. Technol.* **3**, 1800265 (2018).
9. Fassler, A. & Majidi, C. 3D structures of liquid-phase GaIn alloy embedded in PDMS with freeze casting. *Lab Chip* **13**, 4442–4450 (2013).
10. Li, Y. et al. High-fidelity and high-efficiency additive manufacturing using tunable pre-curing digital light processing. *Addit. Manuf.* **30**, 100889 (2019).
11. Liu, J. et al. 3D printing of biomimetic multi-layered GelMA/nHA scaffold for osteochondral defect repair. *Mater. Des.* **171**, 107708 (2019).
12. Boley, J. W., White, E. L., Chiu, G. T.-C. & Kramer, R. K. Direct writing of gallium-indium alloy for stretchable electronics. *Adv. Funct. Mater.* **24**, 3501–3507 (2014).
13. Tabatabai, A., Fassler, A., Usiak, C. & Majidi, C. Liquid-phase gallium-indium alloy electronics with microcontact printing. *Langmuir* **29**, 6194–6200 (2013).
14. Zheng, Y., He, Z.-Z., Yang, J. & Liu, J. Personal electronics printing via tapping mode composite liquid metal ink delivery and adhesion mechanism. *Sci. Rep.* **4**, 4588 (2014).
15. Park, Y.-G., An, H. S., Kim, J.-Y. & Park, J.-U. High-resolution, reconfigurable printing of liquid metals with three-dimensional structures. *Sci. Adv.* **5**, eaaw2844 (2019).
16. Park, Y.-G. et al. Three-dimensional, high-resolution printing of carbon nanotube/liquid metal composites with mechanical and electrical reinforcement. *Nano Lett.* **19**, 4866–4872 (2019).
17. Palleau, E., Reece, S., Desai, S. C., Smith, M. E. & Dickey, M. D. Self-healing stretchable wires for reconfigurable circuit wiring and 3D microfluidics. *Adv. Mater.* **25**, 1589–1592 (2013).
18. Yu, Y., Liu, F., Zhang, R. & Liu, J. Suspension 3D printing of liquid metal into self-healing hydrogel. *Adv. Mater. Technol.* **2**, 1700173 (2017).
19. Neumann, T. V. & Dickey, M. D. Liquid metal direct write and 3D printing: a review. *Adv. Mater. Technol.* **5**, 2000070 (2020).
20. Zrnic, D. & Swatik, D. S. On the resistivity and surface tension of the eutectic alloy of gallium and indium. *J. Less-Common Met.* **18**, 67–68 (1969).
21. Ozutemiz, K. B., Wissman, J., Ozdoganlar, O. B. & Majidi, C. EGaIn-metal interfacing for liquid metal circuitry and microelectronics integration. *Adv. Mater. Interfaces* **5**, 1701596 (2018).
22. Gannarapu, A. & Gozen, B. A. Micro-extrusion-based additive manufacturing with liquid metals and alloys: flow and deposition driven by oxide skin mechanics. *Extrem. Mech. Lett.* **33**, 100554 (2019).
23. Ladd, C., So, J.-H., Muth, J. & Dickey, M. D. 3D printing of free standing liquid metal microstructures. *Adv. Mater.* **25**, 5081–5085 (2013).
24. Eggers, J. & Villermaux, E. Physics of liquid jets. *Rep. Prog. Phys.* **71**, 036601 (2008).
25. Jacob, A. R., Parekh, D. P., Dickey, M. D. & Hsiao, L. C. Interfacial rheology of gallium-based liquid metals. *Langmuir* **35**, 11774–11783 (2019).
26. Daalkhaijav, U., Yirmibesoglu, O. D., Walker, S. & Mengüç, Y. Rheological modification of liquid metal for additive manufacturing of stretchable electronics. *Adv. Mater. Technol.* **3**, 1700351 (2018).
27. Gannarapu, A., Dutta, P. & Gozen, B. A. Prediction of steady-state freeze front position during 3D printing of microstructures. *Int. J. Heat. Mass Transf.* **115**, 743–753 (2017).
28. Yin, J., Zhao, D. & Liu, J. Trends on physical understanding of bioink printability. *Bio-Des. Manuf.* **2**, 50–54 (2019).
29. Hinton, T. J. et al. Three-dimensional printing of complex biological structures by freeform reversible embedding of suspended hydrogels. *Sci. Adv.* **1**, e1500758 (2015).
30. Jin, Y., Chai, W. & Huang, Y. Printability study of hydrogel solution extrusion in nanoclay yield-stress bath during printing-then-gelation biofabrication. *Mater. Sci. Eng. C.* **80**, 313–325 (2017).
31. Grosskopf, A. K. et al. Viscoplastic Matrix Materials for Embedded 3D Printing. *ACS Appl. Mater. Interfaces* **10**, 23353–23361 (2018).
32. Hinton, T. J., Hudson, A., Pusch, K., Lee, A. & Feinberg, A. W. 3D printing PDMS elastomer in a hydrophilic support bath via freeform reversible embedding. *ACS Biomater. Sci. Eng.* **2**, 1781–1786 (2016).
33. Muth, J. T. et al. Embedded 3D printing of strain sensors within highly stretchable elastomers. *Adv. Mater.* **26**, 6307–6312 (2014).
34. Wang, X. et al. Electrochemically enabled embedded three-dimensional printing of freestanding gallium wire-like structures. *ACS Appl. Mater. Interfaces* **12**, 53966–53972 (2020).
35. Nelson, A. Z., Kundukad, B., Wong, W. K., Khan, S. A. & Doyle, P. S. Embedded droplet printing in yield-stress fluids. *Proc. Natl Acad. Sci. USA* **117**, 5671–5679 (2020).
36. Beris, A. N., Tsamopoulos, J. A., Armstrong, R. C. & Brown, R. A. Creeping motion of a sphere through a Bingham plastic. *J. Fluid Mech.* **158**, 219–244 (1985).
37. O'Bryan, C. S. et al. Three-dimensional printing with sacrificial materials for soft matter manufacturing. *MRS Bull.* **42**, 571–577 (2017).
38. Cai, L., Marthelot, J. & Brun, P.-T. An unbounded approach to microfluidics using the Rayleigh-Plateau instability of viscous threads directly drawn in a bath. *Proc. Natl Acad. Sci. USA* **116**, 22966–22971 (2019).
39. Teng, L. et al. Soft radio-frequency identification sensors: wireless long-range strain sensors using radio-frequency identification. *Soft Robot* **6**, 82–94 (2019).
40. Huang, X. et al. Materials and designs for wireless epidermal sensors of hydration and strain. *Adv. Funct. Mater.* **24**, 3846–3854 (2014).
41. Hassan, R. S., Lee, J. & Kim, S. A minimally invasive implantable sensor for continuous wireless glucose monitoring based on a passive resonator. *IEEE Antennas Wirel. Propag. Lett.* **19**, 124–128 (2020).
42. Charkhabi, S. et al. Kirigami-enabled, passive resonant sensors for wireless deformation monitoring. *Adv. Mater. Technol.* **4**, 1800683 (2019).
43. Yin, J., Yan, M., Wang, Y., Fu, J. & Suo, H. 3D bioprinting of low-concentration cell-laden gelatin methacrylate (GelMA) bioinks with a two-step cross-linking strategy. *ACS Appl. Mater. Interfaces* **10**, 6849–6857 (2018).
44. Li, Y. et al. Theoretical prediction and experimental validation of the digital light processing (DLP) working curve for photocurable materials. *Addit. Manuf.* **37**, 101716 (2021).

ACKNOWLEDGEMENTS

The authors gratefully acknowledge the support provided by the National Key Research and Development Program of China (Grant No. 2018YFA0703000), the National Natural Science Foundation of China (Grant Nos. 52075482, 12125205, 12072316, and 51973189), and the Starry Night Science Fund of Zhejiang University Shanghai Institute for Advanced Study (Grant No. SN-ZJU-SIAS-004).

AUTHOR CONTRIBUTIONS

Q.W. and F.Z. conducted the experiments, analyzed the data, and wrote the manuscript. Z.W. and Y.X. provided the support bath materials and conducted the characterization of the sensors. J.Q. and J.Y. conceived the concept of this work. J.Y. and H.Y. oversaw all the research phases and revised the manuscript. All authors discussed and commented on the manuscript.

COMPETING INTERESTS

The authors declare no competing interests.

ADDITIONAL INFORMATION

Supplementary information The online version contains supplementary material available at https://doi.org/10.1038/s41528-022-00184-6.

Correspondence and requests for materials should be addressed to Ziliang Wu, Jin Qian or Jun Yin.

Reprints and permission information is available at http://www.nature.com/reprints

Publisher's note Springer Nature remains neutral with regard to jurisdictional claims in published maps and institutional affiliations.